doi:10.26443/seismica.v5i1.2108

The 2022 hydraulic stimulation at Utah FORGE: investigating fracturing mechanisms and testing forecasting approaches

Federica Lanza [*1], **Antonio P. Rinaldi** [1], **Luigi Passarelli** [2], **Vanille A. Ritz** [1], **Victor Clasen Repollés** [1], **Ryan Schultz** [1], **Federico Ciardo** [3], **Laura Ermert** [5], **Luca Scarabello** [10], **Nicolas Schmid** [1], **Peidong Shi** [11], **Katinka Tuinstra** [1], **Arnaud Mignan** [6], **Ben Dyer**[4], **Dimitrios Karvounis** [4], **Peter Meier**[4], **Kristine Pankow** [7], **Jim Rutledge**[8], **Joseph Moore**[9], **Stefan Wiemer** [1]

[1]Swiss Seismological Service, ETH Zürich, Switzerland, [2]INGV Bologna, Italy, [3]Northwestern University, USA, [4]Geo-Energie Suisse, Switzerland, [5]Univ. Grenoble Alpes, Univ. Savoie Mont Blanc, CNRS, IRD, Univ. Gustave Eiffel, ISTerre, France, [6]Mignan Risk Analytics GmbH, Switzerland, [7]University of Utah Seismograph Stations, UT, USA, [8]Santa Fe Seismic, NM, USA, [9]Energy and Geoscience Institute, University of Utah, UT, USA, [10]Department of Earth and Planetary Sciences, ETH Zürich, [11]Cardiff University, UK

Author contributions: *Conceptualization*: F. Lanza, A. P. Rinaldi, L. Passarelli. *Data Curation*: B. Dyer, P. Meier, D. Karvounis. *Formal analysis*: A. P. Rinaldi, L. Passarelli, V. A. Ritz. *Funding Acquisition*: S. Wiemer, A. P. Rinaldi. *Investigation*: F. Lanza, A. P. Rinaldi, L. Passarelli, V. A. Ritz, V. Clasen Repollés, R. Schultz. *Software*: N. Schmid, L. Scarabello, A. P. Rinaldi, V. Clasen Repollés. *Visualization*: F. Lanza, A. P. Rinaldi, L. Passarelli, V. A. Ritz, V. Clasen Repollés. *Writing – original draft*: F. Lanza, A. P. Rinaldi, L. Passarelli. *Writing – review & editing*: all co-authors.

Abstract Managing induced seismicity risk is needed to enable the widespread adoption of geothermal technologies, facilitating the transition towards a decarbonized energy sector. In April 2022, real-time monitoring and forecasting of induced seismicity were tested during a three-stage hydraulic stimulation in a deep granite heat reservoir at the Utah FORGE site. Here, we analyze the recorded seismicity through statistical inference, and investigate the possible fracturing mechanisms triggered by the injection operation. Our analysis indicates that seismicity is likely induced by opening of a tensile fracture. Through pseudo-prospective forecasting, we then replay the Stage 3 stimulation and related induced seismicity as if it were happening in real-time. We demonstrate that even if the physical processes are complex and likely difficult to disentangle using seismicity alone, physics-based seismicity rate forecasting models show promise for stable forecastability of seismicity induced during hydraulic stimulation. Our results pave the way for Advanced Traffic Light Protocols (ATLP) to become standard operational technology in the mitigation strategies of deep geothermal projects.

Non-technical summary Geothermal energy has great potential to provide clean and renewable power, but developing deep geothermal systems can sometimes trigger small, human-induced earthquakes. Understanding and managing this induced seismicity is key to ensuring that geothermal energy remains both safe and sustainable. In this study, we analyze seismic activity from a hydraulic stimulation experiment carried out in 2022 at the Utah FORGE research site, where water was injected into hot granite to enhance heat extraction. By analyzing the recorded earthquakes, we identify the likely fracturing mechanisms caused by the injection and find that most of the seismicity was linked to the opening of small cracks in the rock. We also test models designed to forecast seismic activity as it happens in real time. Despite the complexity of the physical processes involved, these models show strong potential for reliable forecasting. Our results highlight how physics-based forecasting tools can support risk management strategies for future geothermal projects, an important step toward a cleaner energy future.

Production Editor: Yen Joe Tan
Handling Editor: Giuseppe Petrillo
Copy & Layout Editor: Théa Ragon

Signed reviewer(s): Jinping Zi, and an anonymous reviewer with the help of Lichun Yang

Received: November 3, 2025
Accepted: March 25, 2026
Published: April 8, 2026

1 Introduction

Enhanced geothermal systems (EGS, Olasolo et al., 2016; Horne et al., 2025) promise to become an abundant decarbonized energy source for heating and baseload power, representing a key technology to combat climate change. However, the widespread roll-out of EGS is challenged by closely interrelated concerns about induced earthquakes, decreasing societal acceptance, and economic viability due to insufficient production rates and high costs (Mignan et al., 2019). To develop an EGS reservoir, permeability is generally enhanced by hydraulic stimulation (Jia et al., 2022), where fluids are injected under high pressure to cause the rock mass to fail (by shearing or fracturing), thereby improving fluid circulation at depth. Thus, induced micro-seismicity is not an undesired by-product, but a necessary tool to create a productive heat exchanger in low-permeability reservoirs (Majer et al., 2007). If, however, the stimulated fractures interact with pre-existing fault systems, the increase in pore fluid pressure could potentially induce earthquakes of significant size (Schultz et al., 2020; Moein et al., 2023). The

*Corresponding author: federica.lanza@sed.ethz.ch

impact of such larger earthquakes (e.g., the 2006 M_L 3.4 in Basel, Switzerland (Häring et al., 2008), the 2017 M_w 5.5 earthquake in Pohang, South Korea (Grigoli et al., 2017) and the 2021 M_L 3.4 earthquake in Strasbourg, France (Schmittbuhl et al., 2022)) on geothermal projects worldwide is tremendous, with ripple effects on decreased public and political support for the technology.

Thus, it is imperative that efforts are focused on the development of strategies, tools, and guidelines to assess, manage, and reduce the seismic risk (Trutnevyte and Wiemer, 2017; Grigoli et al., 2017; Zhou et al., 2024; Schultz et al., 2025, 2022). In particular, the physical interpretation of the geothermal reservoir evolution, together with robust real-time seismic monitoring and forecasting, is paramount to understand the seismicity response of the host rocks during an EGS operation.

Through the analysis of seismicity catalogs, hydraulic parameters, and in-situ stress we can constrain the geometry and kinematics of possible physical mechanisms. Examples of state-of-the-art physical source models are opening (and shearing) of structures either by tensile or mixed mode cracks (e.g., Nikkhoo et al., 2016; Davis et al., 2020; Möri and Lecampion, 2023) or seismic/aseismic shearing caused by the injection operation (Cappa et al., 2019; Danré et al., 2024). The fracturing/slip mechanisms can be modelled via hybrid-stochastic (Rinaldi and Nespoli, 2017; Ritz et al., 2022; Clasen Repollés et al., 2025) and physics-based approaches (Rinaldi and Rutqvist, 2019; Zbinden et al., 2020; Vaezi et al., 2024), both allowing inferences into the seismological response rooted in physical processes. However, computational demand limits their applicability in a real-time scenario, especially considering the time needed for complex parameter estimates through inverse modeling. Alternatively, simpler and faster approaches are statistical forecasting models (Shapiro et al., 2010; Bachmann et al., 2011; Mignan et al., 2017; Broccardo et al., 2017; Grigoratos et al., 2022; Ritz et al., 2024) which, however, have poor capability to discern the physical mechanisms. More recently, machine learning models (Yu et al., 2023; Mignan et al., 2024) have also shown promise due to their flexibility to deal with multi-variate problems where no clear patterns are observable (Jordan and Mitchell, 2015). Data-driven multi-model approaches offer the possibility to run different models even with limited computational resources and to combine their weighted outputs, minimizing the specific biases of each model. The use of a fast forecasting tool is essential for the development of Advanced Traffic Light Protocols (ATLP) that rely on model forecasts to compute hazard or even risk, thus helping to provide a probabilistic assistance to the operator's decision-making (Schultz et al., 2021; Király-Proag et al., 2017).

Here, leveraging the stimulation activities conducted at the Utah FORGE geothermal testbed site (Moore et al., 2019, 2023; Jones et al., 2024), we first discuss the main temporal and spatial features related to the induced seismicity recorded during the 2022 injection operations. We investigate the possible fracturing mechanisms triggered by the stimulations by fitting three plausible physical models, i.e. a high-pore pressure diffusion model, an aseismic crack model, and a tensile crack model as the causative process of the recorded seismicity. Finally, we explore the potential of data-driven statistical and machine learning models to forecast the evolution of induced seismicity. We replay the 2022 induced seismicity sequences through pseudo-prospective forecasting. We demonstrate that despite the complexity and difficulty in isolating the physical processes using seismicity alone, a physics-based stochastic approach shows promise to reliably forecast the occurrence of induced events. We then discuss our findings in the context of the emerging ATLP and implementation of risk-based frameworks, as a viable pathway to de-risking geothermal projects.

2 Utah FORGE

The U.S. Department of Energy Utah FORGE is a dedicated international underground field-scale laboratory in Utah. Its purpose is to develop, test, and accelerate breakthroughs in EGS projects regarding drilling techniques, injection strategies, earthquake monitoring, risk communication, and prove that safe and sustainable development of geothermal energy in the deep underground is possible (Moore et al., 2019, 2023; Pankow et al., 2020; Wannamaker et al., 2020; Ramadan et al., 2026). Utah FORGE is located in a sparsely populated area on the western flank of the Mineral Mountains in the vicinity of Milford in Beaver County, Utah, a small community of ~1,400 people (Figure 1). It is close to the active Blundell geothermal plant in the Roosevelt Hot Springs (Gwynn et al., 2016; Jones et al., 2024) within Utah's Renewable Energy corridor. Utah FORGE sits on alluvial fan deposits of 300-1000 m in thickness with the target EGS reservoir created in the underlying basement granitoid rocks, where temperatures exceed 190°C at less than 3 km depth. The stress field of the FORGE site has been studied in detail by Xing et al. (2022) using the fracture orientation and breakouts of the log data of the first drilled deviated well 16A (78)-32. The azimuthal orientation of the tensile fractures indicates an NNE-SSW general trend of S_{Hmax} with a variability between N10°E-N50°E that is compatible with a N25°E orientation of the regional S_{Hmax}. Well log analysis suggests a 25° clockwise rotation of the principal stress axes around S_{Hmax}, with the stress magnitude of S_v = 62-65 MPa, S_{Hmin} = 40-45 MPa and S_{Hmax} = 47-78 MPa estimated at true vertical depth of 2,500 m given the stress depth gradients derived by Xing et al. (2022). The range of variability of S_{Hmax} implies the possibility of a transition between S_v and S_{Hmax} as maximum principal stress, with a consequent change from normal to strike-slip faulting regime.

Between April 17 and 21, 2022, a stimulation of well 16A (78)-32 (Figure 1) was conducted in three consecutive stages (McLennan et al., 2023; Niemz et al., 2024) with the purpose of demonstrating reservoir growth and providing seismic imaging to guide the location of the drilling of the production well (16B (78)-32), which was not yet drilled at that time. During the stimulation, a total of ~1,600 m^3 pressurized fluids were in-

	Manual catalog			
	Number of events	Mc (MAXC+0.2) (M_w)	b-value	N ≥ Mc
Stage 1	823	-1.09	1.95 ± 0.16	126
Stage 2	1322	-1.29	1.36 ± 0.04	658
Stage 3	5283	-1.19	1.14 ± 0.02	2438

Table 1 Overview of the statistical analysis of the manually inspected catalog.

jected into the target reservoir at ~2.4 km depth through open-hole and perforated intervals, following stepwise pressure increases followed by rapid shut-ins, reaching maximum pressures of 42.3–49.8 MPa. For additional operational details of the injection, please refer to Text S1 in the Supplementary Materials. Seismic monitoring relied both on a surface network of five surface broadband stations (red triangles in Figure 1), three accelerometers, of which one was placed in a shallow well (68-32) operated by the University of Utah Seismograph Stations (University of Utah, 1962), a temporary high-density nodal array arranged in dense rectangular patches covering the footprint of the Utah FORGE site (Whidden et al., 2023), and surface fiber optics (Distributed Acoustic Sensing, DAS) (Moore et al., 2023). In addition, three deep boreholes (> 1.6 km) were equipped with downhole geophone strings and fiber-optic cable for DAS that allowed precise location of induced microseismicity (Moore et al., 2023; Rutledge et al., 2022; Dyer et al., 2023a). Not all the geophones were operational during the first two stages, and the monitoring network was fully operational only during the third stage.

For our study, we use the downhole catalog of Dyer et al. (2023b), which contains 21,937 located microseismic events: 7,428 events were manually checked across all three stages, while 14,509 events are generally smaller, poorly located, and with approximate magnitude estimates that were obtained with automatic bootstrapping methods. The results presented here relate to the manually inspected events, which yields the highest quality in terms of both locations and magnitude calculation (Figures 2, S1). The results for all the events with assigned magnitudes and irrespective of the quality of their locations are reported in the Supplementary Information (see Figure S2 and Table S1). During stages 1-3, the largest events were M_w -0.10, -0.23, and 0.62, respectively.

3 Methods

3.1 Calculation of Magnitude of completeness (Mc) and b-value evolution in time

The magnitude of completeness is assessed using the Maximum curvature method as described in Wiemer (2000). This method defines the completeness threshold of a catalog as the point of maximum curvature of the non-cumulative frequency-magnitude curve. This robustness and ease of applicability of the method, however, tends to underestimate Mc, especially for gradually curved frequency-magnitude distributions (e.g., for catalogs with a fine magnitude binning or catalogs with a small magnitude range). To avoid this underestimation, we apply a commonly used correction of +0.2 M_w (Woessner and Wiemer, 2005). The corrected maximum curvature provides a robust and not overly conservative estimate for all the stages investigated. The *b*-value is then estimated using the maximum-likelihood estimate with correction for binning (Marzocchi and Sandri, 2009).

To estimate the temporal variation of the *b*-value, we use a moving window with a length set to a fixed number of events and a 10% overlap. Different window sizes have been tested (see Figure S3), and the results presented in the main article are for 200 events ≥ Mc (except for stage 1, as it has only 100 events above completeness). In each window, Mc is set to the value corresponding to that stage (Table 1), ensuring the same number of events across all windows. A comparison of the temporal evolution of the *b*-value obtained using a fixed Mc versus a variable Mc for each window reveals that the overall patterns and values remain largely similar between the two approaches (Figure S4). In Figure 2b, c, d, the *b*-value of each subset is plotted at the time of the last event of the subset-catalog. A more recent approach to calculate the *b*-value (b+) with less bias linked to short-term aftershock incompleteness (STAI) shows little difference in the overall patterns of transient *b*-values for the three stages investigated, suggesting that STAI is not affecting the catalog in FORGE (Figure S5). The statistical parameters of the catalog (Mc, *b*-value and error on *b*-value) are estimated using the SeismoStats package (Mirwald et al., 2025).

3.2 Derivation of the seismicity cloud's spatial features with Principal Component Analysis (PCA)

Principal Component Analysis (PCA) is generally used for dimensionality reduction and consists of finding a new coordinate system in the data space described by an orthonormal basis, the principal components, obtained as eigenvector of the data covariance matrix or via singular value decomposition of the data matrix (Jolliffe and Cadima, 2016). In our three-dimensional application, PCA fits an ellipsoid from the distribution of earthquake coordinates. The axes of the ellipsoid are the principal components, i.e. eigenvectors in the data space, scaled by the eigenvalues that give the variance of the data along each axis. A small value of any axis of the ellipsoid implies a small variance of the data along that direction, i.e., the ellipsoid can collapse to a plane or even a line when one or two of the three axes are small (Quinn and Ehlmann, 2019). This technique infers the best-fit geometrical shape of the earthquake hypocenter

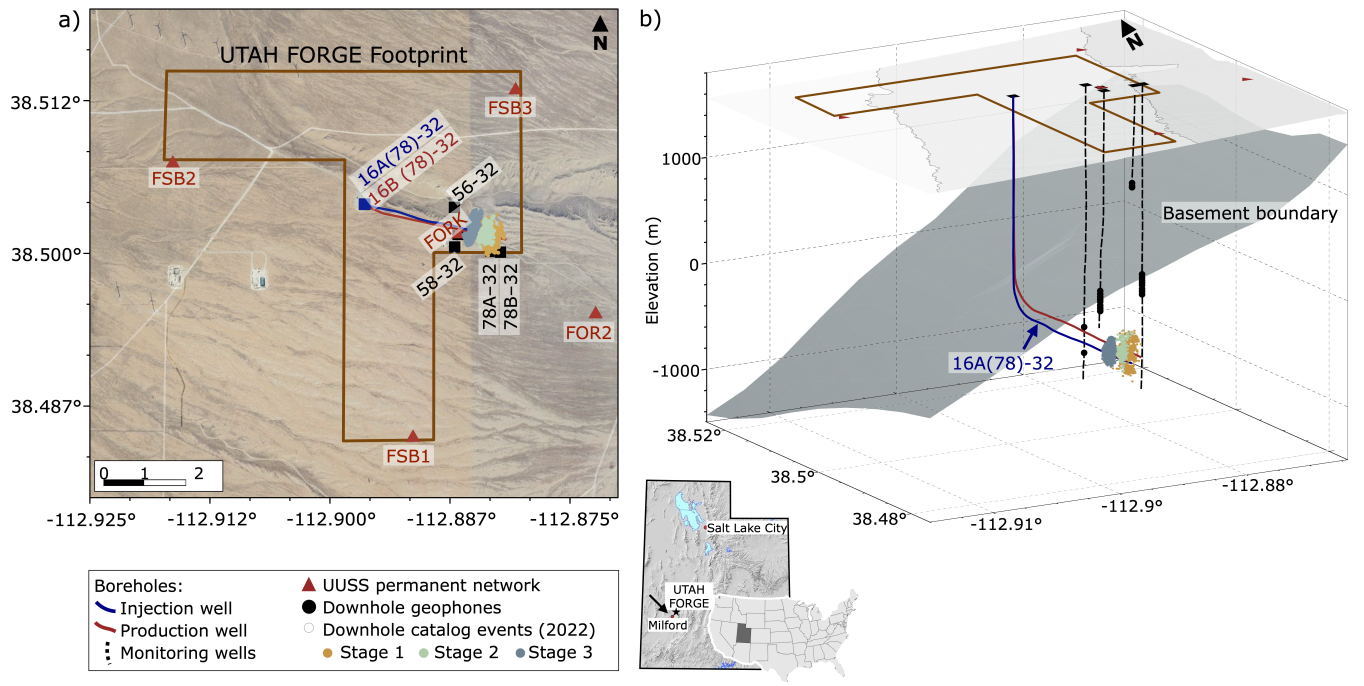

Figure 1 a) Map of the Utah FORGE geothermal site, in Utah, USA. The high-quality manually checked events recorded during the 2022 Utah FORGE stimulation are shown with solid circles, color-coded by stage. The blue square illustrates the surface location of the stimulation well (16A (78)-32). All wells drilled to date (78A-32, 78B-32, 68-32, 56-32, 16A (78)-32, 16B (78)-32) are indicated by black squares, while the seismic stations of the seismic network currently active are shown with red triangles. b) 3D rendition of the site highlighting the dipping granitoid layer (dark gray surface), the injection well 16A (78)-32 (blue line), the production well 16B (78)-32 (red line), and the instrumented monitoring wells 78-32, 56-32, and 58-32 (dashed black lines); at the surface, topography is indicated by contours lines.

distribution as ellipsoidal, planar, or linear structures. Please refer to Quinn and Ehlmann (2019) and Supplementary Text S1 for a detailed derivation of the PCA in the case of a 3D distribution of data points.

We computed the PCA using the singular value decomposition implemented in the Matlab routine *svd* for Stage 3 only. We used all manually revised earthquakes above magnitude M_w = -1.5 to prevent small and probably less well-located events from introducing noise into the fit. The fitted ellipsoid has 1 standard deviation axis, i.e. singular values, s_i = (74.9, 54.7, 16.5) m, which corresponds to proportion of variance $\pi_i = (0.63, 0.33, 0.03)$. Therefore, the analysis suggests that the distribution of seismicity is planar since the variance in the direction orthogonal to the plane is only 3%. In this case, the first and second column eigenvectors of u_1 and u_2 define the plane, and the third eigenvector $u_3 = (u_{13}, u_{23}, u_{33})$ is the vector orthogonal to the plane and defines univocally the equation of the plane in the earthquake coordinate system $u_3 \bullet x + u_3 \bullet \mu_X = 0$, where μ_X is the earthquake hypocenter centroid and x a set of spatial coordinates. The geometry of the plane in strike and dip geological convention can be easily calculated by projecting the normal vector (positive upwards) to the fitted plane onto a horizontal plane and the depth axis, for strike and dip angles, respectively, and obtaining (Quinn and Ehlmann, 2019):

$$(strike, dip) = (\tan^{-1}\frac{u_{13}}{u_{23}} - \frac{\pi}{2}, \cos^{-1}\frac{u_{33}}{\|u_{33}\|}) \quad (1)$$

3.3 Fracturing mechanisms models

Here, we briefly describe three plausible physical models that we considered as the causative process of the recorded seismicity: (1) a penny-shaped tensile crack model, (2) a high pore-pressure diffusion model, and (3) an aseismic crack model.

Fitting a penny-shaped tensile crack model. To fit the time and space evolution of seismicity, we use a simple penny-shaped crack model and assume that seismicity is triggered at the expanding edges of the 3D crack. In this way, the earthquake migrating front ($R(t)$) tracks the expansion of the penny-shaped crack of radius a. For such crack geometry (Davis et al., 2020), the volume of the tensile fracture is proportional to the crack radius according to the equation (Tada et al., 2000):

$$V_{crack} = \frac{8(1-\nu)}{3\mu} p_0 a^3 = k_{psc} a^3 \quad (2)$$

where, n and m are the Poisson ratio and the rock rigidity, respectively, and p_o is the overpressure inside the tensile crack, crack, $k_{psc} = \frac{8(1-\nu)}{3\mu} p_0$. Assuming that there is no leak-off and all the volume injected acts as an expanding the crack we can assume that $V_{crack}(t) = V_{inj}(t)$ and obtain a model that links the migrating front of earthquakes and the volume injected through time:

$$R(t) = (\frac{V_{inj}(t)}{k_{psc}})^{\frac{1}{3}} \quad (3)$$

The model has radial symmetry and depends on the injected volume $V_{inj}(t) = \int_o^t Q(t')dt'$,where $Q(t)$ is the injection rate and t is the time from the injection onset.

Fitting a high-pore pressure diffusion model. The seismicity evolution in space and time could occur on an already existing fault, where seismic slip is triggered by pressurization of the fault due to the volume injected. Earthquakes could thus be triggered by an increase in the pore-pressure that lowers effective normal stress and yield asperity to slip if they are already in a critical stress state according to the Mohr-Coulomb failure criterion (Parotidis et al., 2003; Talwani and Acree, 1984). Assuming pore-elasticity and a pulse-like pressure perturbation, it has been calculated that the seismicity front will migrate with a parabolic diffusion-like profile in a spatiotemporal evolution according to

$$R(t) = (4\pi D_f t)^{\frac{1}{2}} \tag{4}$$

where D_f is the seismic diffusivity coefficient for the earthquake migrating front and t is the time from the injection onset (Shapiro et al., 1997). Additionally, with the same previous modelling assumptions, at the end of the injection operation, a back-front of seismicity shadow develops with a functional shape given by (Parotidis et al., 2004):

$$R(t) = (6D_{bf}t\left(\frac{t}{t_e} - 1\right)\ln\left(\frac{t}{t - t_e}\right))^{\frac{1}{2}} \tag{5}$$

where t_e is the time of the end of the injection operation, and D_{bf} is the diffusivity of the earthquake migrating back-front.

Fitting an aseismic crack model. In recent years, it has been shown that injection of pressurized fluids into fault structures can also induce aseismic slip together with the occurrence of regular earthquakes (Guglielmi et al., 2015). The volume injected on a fault can cause fault unclamping and create the condition for an aseismic rupture to start (Cappa et al., 2019; Lengliné et al., 2017). The stress concentration at the propagating aseismic rupture edges can trigger seismicity on brittle asperities punctuating the fault (Cappa et al., 2019). A recently developed model describes this process as an aseismic shear crack induced by the fault pressurization that propagates along the fault plane punctuated by velocity weakening asperities (Danré et al., 2024). The latter slips seismically when overrun by the aseismic rupture front. This model thus predicts a parabolic dependence of the distance of the earthquake migrating front with the volume injected as

$$R(t) = (k_d V_{inj}(t))^{\frac{1}{2}} \tag{6}$$

where k_d is a parameter that depends on fault and fluid properties (Danré et al., 2024). A similar empirical model that uses simpler assumptions but with a similar volume distance functional form is also presented in Lengliné et al. (2017).

3.4 Mohr-Coulomb Criterion

The Coulomb-Mohr failure criterion states that slip occurs when the shear stress is higher than the effective normal stress minus the cohesion coefficient on the source fault:

$$\tau > f_s \sigma_n^{eff} - C_o \tag{7}$$

where f_s is the coefficient of internal friction, and $\sigma_n^{eff} = \sigma_n - P$, is the normal stress minus the pore-pressure P. Here, we evaluate this criterion using the Mohr circle representation of shear and effective normal stress on the fault given the in-situ principal stress magnitude, for normal hydrostatic condition, and by accounting for the overpressure induced by the injection operation.

3.5 Forecasting models

Despite their relative importance, the occurrence of physical mechanisms (e.g., crack vs. aseismic) has not yet been quantified in the context of hazard. Hence, in the context of ATLP, we limited testing to three different models in which we incrementally account for the physics of pore pressure propagation. The three models (Empirical, Physics-Informed Machine Learning, and Stochastic Hydro-mechanical) are chosen as candidates for ATLP; these models are relatively simple and computationally efficient, allowing for a large number of simulations.

The first model is purely empirical (referred to as EM) and simply links injection rate with seismicity rate (i.e., the seismogenic index model - Shapiro et al., 2010; Shapiro, 2015; Kwiatek et al., 2024), where the model parameters are estimated via a Maximum Likelihood Estimate (Broccardo et al., 2017; Clasen Repollés et al., 2025).

The second model, a Physics-Informed Machine Learning model (PI-ML), is a modified version of the multi-LASSO model presented by Mignan et al. (2024). In addition to the data-driven time series (e.g. flow rate, pressure, seismicity-rate, as well as their derivates and combinations), and the planned flow-rate in the forecasting period, we added time series of the forecasted pressure evolution based on standard analytical solutions: given a particular dataset at time t_{learn}, we invert these analytical solutions for the pressure propagation. The calibrated flow model is then run for $t > t_{learn}$, and the solution used to produce a seismicity forecast. For these solutions, permeability and porosity are assumed constant. More details about the analytical solutions can be found in Clasen Repollés et al. (2025). Introducing additional time series in the forecast part provides the m-LASSO model with further information and potentially better forecast (e.g. allowing to easily reproduce decay of seismicity during shut-in). The physics-informed approach also allows us to easily simulate a multi-cycle approach for the same injection stage as it easily accounts for the pressure variation between cycles. For multi-stage, the weights between time-series may vary.

Finally, the third model is a 1D hybrid-hydromechanical approach recently developed by

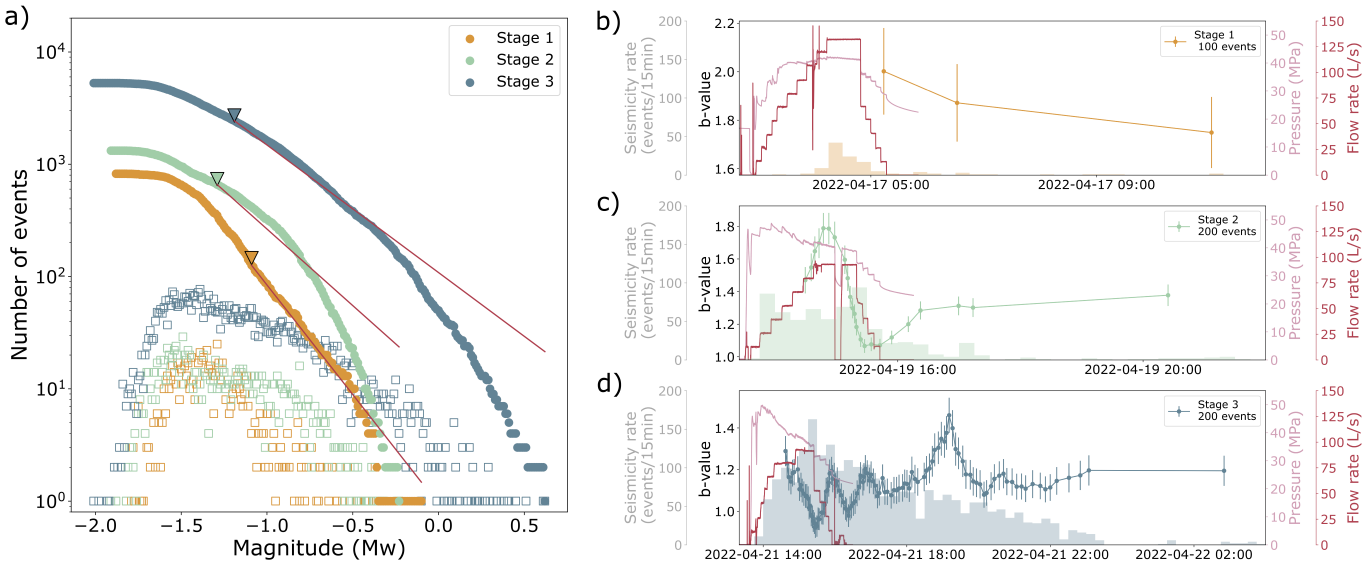

Figure 2 Statistical analysis of the manually inspected catalog. a) Frequency-magnitude distribution. Inverted triangles denote the estimated magnitude of completeness for each stage. b-d) Temporal evolution of the *b*-value and injection rate for stage 1, 2 and 3 (100 or 200 events window with completeness pre-filter), seismicity rate in 15 minutes bins, and hydraulic data (pressure and flow rate).

Clasen Repollés et al. (2025). The developed package allows the use of different fluid flow models; in this work, we use a 1D numerical fluid flow solution with both reversible and irreversible permeability changes. Elastic effects are simulated following a Barton-Bandis aperture model (Barton et al., 1985), while irreversible effects in aperture are accounted for once a threshold pressure is exceeded (Clasen Repollés et al., 2025). The final permeability is calculated as a function of the aperture following a parallel plate model (Zimmerman and Bodvarsson, 1996). Seismicity can be simulated with two approaches: one based on an analytical derivation (CAPS model) and the second one based on a Monte Carlo approach (SEED model). Here, we opted to use the faster CAPS approach (originally referred to as HM1d$_{num}$-CAPS, here in short as HM1D), generally a preferred choice in real-time forecasting scenarios. More details about the implementation, as well as several tests for different datasets at different scales can be found in Clasen Repollés et al. (2025). While the model HM1D does not account explicitly for penny-shaped tensile crack model and/or aseismic crack model, we considered it analogous in terms of physical complexity as it accounts for permeability changes on pressure threshold (i.e. equivalent to tensile opening) and seismicity based on a Mohr-Coulomb criterion.

For testing the model, we employed a pseudo-forecasting approach (e.g. Ritz et al., 2024), in which we gradually fed the models with new information. The models are unaware of the recorded pressure and seismicity after t_{learn} with the exception of the planned (actually recorded in this case) flow rate. Statistical testing is done by means of a generalized N-test and by comparing the probability gain with respect to the simplest EM model. The generalized N-test checks how well a given model is able to reproduce the final recorded number of events above completeness and gives information on how much data is needed before this is achieved. The probability gain instead compares for each run in the pseudo-forecast test how well a model performed with respect to EM in reproducing the observed rate of seismicity after t_{learn}. More details about the testing strategy can be found in Clasen Repollés et al. (2025). We performed two pseudo-forecast tests: the first by providing the model with a fixed magnitude of completeness (Mc) defined a-priori on the full seismicity dataset, and the second one in which each model computes the Mc based on the data fed.

All the model parameters for the different models are provided in the Supplementary Information in Table S2.

4 Results

4.1 Temporal evolution of the Gutenberg-Richter *b*-value

We computed the *b*-value temporal evolution of the catalogs for each of the three stages (Table 1, Figure 2a). Stage 1 (Figure 2b), performed in the open part of the well in a 60-m-long interval, does not have enough events to draw conclusions and displays very high *b*-values which could be artificially inflated from the large incompleteness of the monitoring network. In Stage 2, we observe an increase in the *b*-value during the ramp-up phase of the injection, followed by a sharp decrease starting around the time of the sudden stop in the injection (Figure 2c). This behavior closely resembles the modelled behavior of seismicity during the propagation of a pressure front in a homogeneous reservoir, with an increase in the *b*-value during the injection phase, followed by a decay of the *b*-value after shut-in (Ritz et al., 2022). During the injection phase in Stage 3, the *b*-value decreases, which could indicate that seismic events focus on pre-existing faults or fractures (Ritz et al., 2022), before showing a complex behavior during and after the shut-in phase (Figure 2d). This complex post-injection

behavior suggests that physical processes are still happening in the post-shut-in phase, and that Stage 3 is affected by processes beyond just the homogeneous propagation of a pressure front. An increase in the *b*-value after shut-in of Stage 3 could hint at re-triggering of asperities in the vicinity of the injection point (Ritz et al., 2022). For both Stages 2 and 3, the injection occurred through discrete, single cluster perforated intervals in the well casing. For Stages 1 and 2, a friction reducer was added to water (slickwater), while Stage 3 featured the injection of a crosslinked polymer fluid system with micro-proppant to increase fluid viscosity at the temperature of the reservoir (Jones et al., 2023).

4.2 Geometrical distribution of seismicity and its fracturing mechanisms

For Stage 3, given the more complete network and the complex *b*-value time evolution, we further investigate the spatial and temporal evolution of seismicity. Time-distance plots for Stages 1 and 2 are provided in the Supplementary Materials (Figure S6) but not further analyzed here. Throughout the following analysis, we translate the earthquake hypocenters to a Universal Transverse Mercator coordinate system (Cartesian: East, North and Vertical) centered at the check-shot point to roughly have the injection point as origin of the coordinate system. We refer to Figure 3 in the main text and to Movie S1 for a visual representation of the observations described below. The seismicity in Stage 3 started to be recorded around the check-shot point immediately after the start of the injection operation (Figure 3a) with small events with magnitudes ranging between M_w -2.0 and -0.5. Seismic events markedly expanded with a move-out pattern. A minor further expansion is seen in the post-injection phase where the largest magnitude was recorded (Figure 3a). Within an hour from the start of the injection, the hydraulic stimulation ramped up to 58 L/s and 50 MPa - which is larger than the S_{Hmin} needed for fracture propagation. During this time, recorded magnitudes ranged between M_w -2.0 and 0.2. In this stage, the seismic activity mainly concentrated in an elliptical patch of roughly 100 x 100 m^2 and 50 m above and northward of the injection point. Small magnitude events also appear ~100 m offset SW-ward from the injection point and branching off the main cloud (Figure 3b). Then, as the flow rate was kept constant for half an hour and then further increased to ~67 L/s for the next hour, the pressure started to gradually drop to 30 MPa, a slightly lower value than S_{Hmin}. In this phase, the earthquake activity increased both in terms of earthquake counts and magnitude (Figure 3a). The earthquake cloud gradually expanded with a move-out pattern from the two patches previously activated with a slightly more pronounced vertical migration. Large magnitude events (up to M_w ~0.5) occurred in the SW-ward offset branch and upward to the initial seismicity. During this phase, earthquakes started to move sideways and branch off the main central patch in NW- and NE-ward direction forming a wing-like distribution of seismicity visible in map view in Figure 3b and Figure 3c. At about one hour and 45 min from the injection operation onset, the well was shut-in for less than five and a half hours, and then was flowed back (open to atmospheric conditions). The shut-in operation coincided with only a small decrease in the earthquake rate which slowly faded out in the next 16 hours (Figure 3a). After the shut-in, however, the seismicity showed a minor expansion for the next 10 hours primarily in the vertical direction, right above the main central cloud activated at the beginning of the injection. There, earthquakes distributed in a planar patch slightly offset to the East and with an opposite dip compared with the main cloud of seismicity below (Figure 3b, c). This new branch of seismicity hosted the larger earthquakes, up to M_w ~0.6, six hours after the start of operation.

Overall, some general patterns can be observed: (1) Seismicity started around the injection point with small magnitude events and gradually expanded covering a final extension of 300 m in the SSW-NNE direction, 150 m in the ESE-WNW direction, and 300 m in the vertical direction (Figure 3a) – we note that the average location error reported in the catalog is ~40 m; (2) The magnitude of events increased linearly during the injection peaking at M_w ~0.6 after the shut-in and during the flow-back operations (6 hours after the start of operation; Figure S7); (3) The expansion of the seismicity cloud is primarily in the vertical and NNE-ward directions during the injection operation, while after shut-in the migration is more pronounced upward with the occurrence of M_w =0.6 earthquakes in the topmost portion of the cloud (Figure 3b, c); (4) The large magnitude earthquakes occurred always peripherally; and (5) The general trend of the seismicity cloud is NNE-SSW subparallel to the orientation of S_{Hmax} (N25°E), but with two pronounced wing-like lobes of seismicity at the end edges of the main cloud and at different depths.

We then study the first order geometrical features of the seismicity cloud by using the Principal Component Analysis (PCA) on the hypocenter distribution. In our three-dimensional application, PCA results in a fitted plane with strike = N15° -195°E and an ESE dipping plane at an angle of 80° as shown in Figure 3b, c. The strike orientation of the fitted plane is rotated 10° counterclockwise with respect to the N25°E average orientation of S_{Hmax} (Figure 3b, c), but it falls in the range of strike orientations of the tensile fracture measured from the well log data (Xing et al., 2022). The distribution of the seismicity lies within a plane that is sub-parallel to the S_v - S_{Hmax} plane and orthogonal to S_{Hmin}.

Based on these results, we explore three possible scenarios to explain the spatial and temporal evolution of earthquake activity in terms of fracture evolution. In the first scenario, seismicity is the result of the fracturing and stress change due to the opening and growth of a hydro-fracture. Alternatively, the injection operation activates seismic slip on an existing fault, and seismicity occurs as a response of high pore-pressure diffusion that lowers the effective normal stress. Lastly, we consider the case where aseismic slip is induced by fault pressurization that in turn triggers seismicity on a pre-existing fault plane.

For all three models, the fit is performed through a nonlinear least-squares algorithm over the duration of

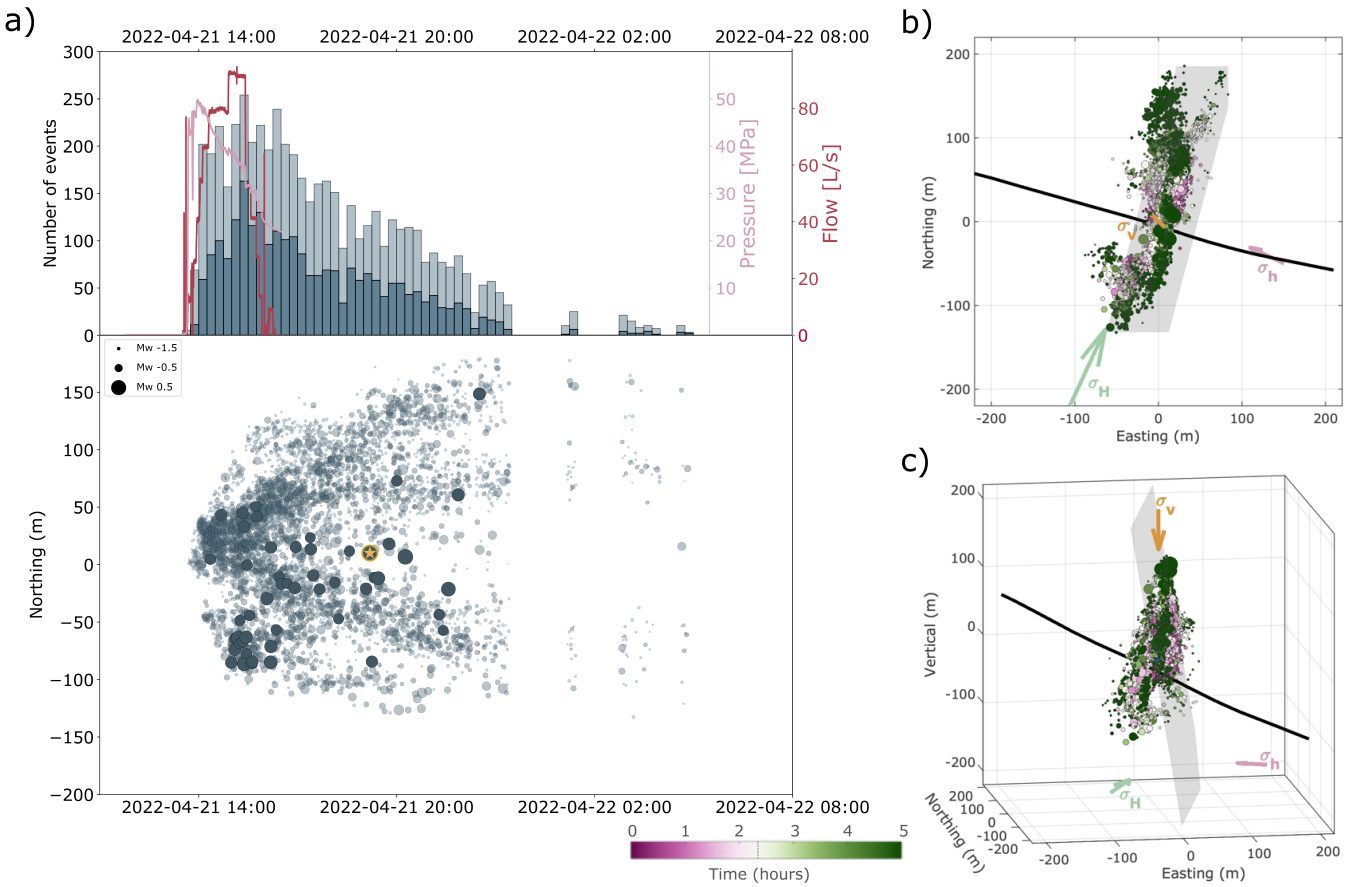

Figure 3 a) Migration of seismicity along Northing direction vs. absolute time of Stage 3. Symbol size and color-code indicate the magnitude of earthquakes; the largest event is marked with a yellow star. Top: Histogram with number of earthquakes in total (light color) and above Mc (dark color) binned every 15 minutes along with flow rate and pressure. b) Map view of the seismicity. c) Three-dimensional distribution of seismicity. Symbols size scales with magnitude and color-code is hours since the start of the injection; the dashed line in the colorbar indicates the shut-in time. Thick black line is the well 16A (78)-32 trajectory and regional principal stresses direction are shown with arrows (Xing et al., 2022). The shaded plane is a best fit plane through PCA analysis, see text for details.

the volume injection operation (three hours), on time bins of 15 minutes in which the average volume and the 99th percentile of the earthquake migrating front are calculated. For the diffusion model, we extend the parabolic curve to ten hours after the start of injection. The fit of the earthquake back-front is performed from the end of the injection operation (2.7633 hours since the start of injection) again using 15-minute time bins and the 1st percentile of distribution of the distance. The best fit parameter of the penny-shaped crack model is $k_{psc} = 0.010(0.009, 0.011)$ with an adjusted R-squared of $\overline{R}^2 = 0.97$. The diffusion model fit returns $D_f = 0.15(0.14, 0.17)\frac{m^2}{s}$ and a $\overline{R}^2 = 0.96$ for the migrating front and $D_{bf} = 0.047(0.038, 0.055)\frac{m^2}{s}$ and a $\overline{R}^2 = 0.12$ for the post-injection phase. The aseismic crack model has the best fit parameters $k_d = 0.86(0.74, 0.99)m^{-1}$ and a $\overline{R}^2 = 0.89$.

The results of the fit of the three models are shown in Figure 4, where volume has been transformed to time to compare the tensile crack and aseismic crack models to the diffusion model which has only time dependence. All three models nicely fit the data during the injection phase as testified from the high values of the adjusted R-squared, where the penny-shaped crack model has a slightly higher value (R^2 = 0.97) compared with the other two models (R^2 = 0.96 and R^2 = 0.89, for the diffusion model and aseismic crack model, respectively). The penny-shaped model better fits the migrating front of earthquakes at the beginning of the injection but slightly underestimates the final distance at the end of the injection, while the aseismic crack model presents the opposite behavior. The diffusion model fits the seismicity front during the injection well but overestimates the evolution of the seismicity front in the post-injection phase. The diffusion model also fits the earthquake back-front poorly, suggesting that pore-pressure diffusion is not the primary mechanism driving the observed space and time evolution of the seismicity. A diffusion model fit (not included in the figure) of the whole migrating front returns a good fit in the post-injection phase but underestimates the migrating front in the first three hours of the injection phase. However, the analysis of the time-distance evolution of the seismicity seems to indicate that the penny-shaped model is the best for modeling the entire injection phase, although the high pore pressure diffusion model fits better the first hour of injection phase and has a comparable R^2.

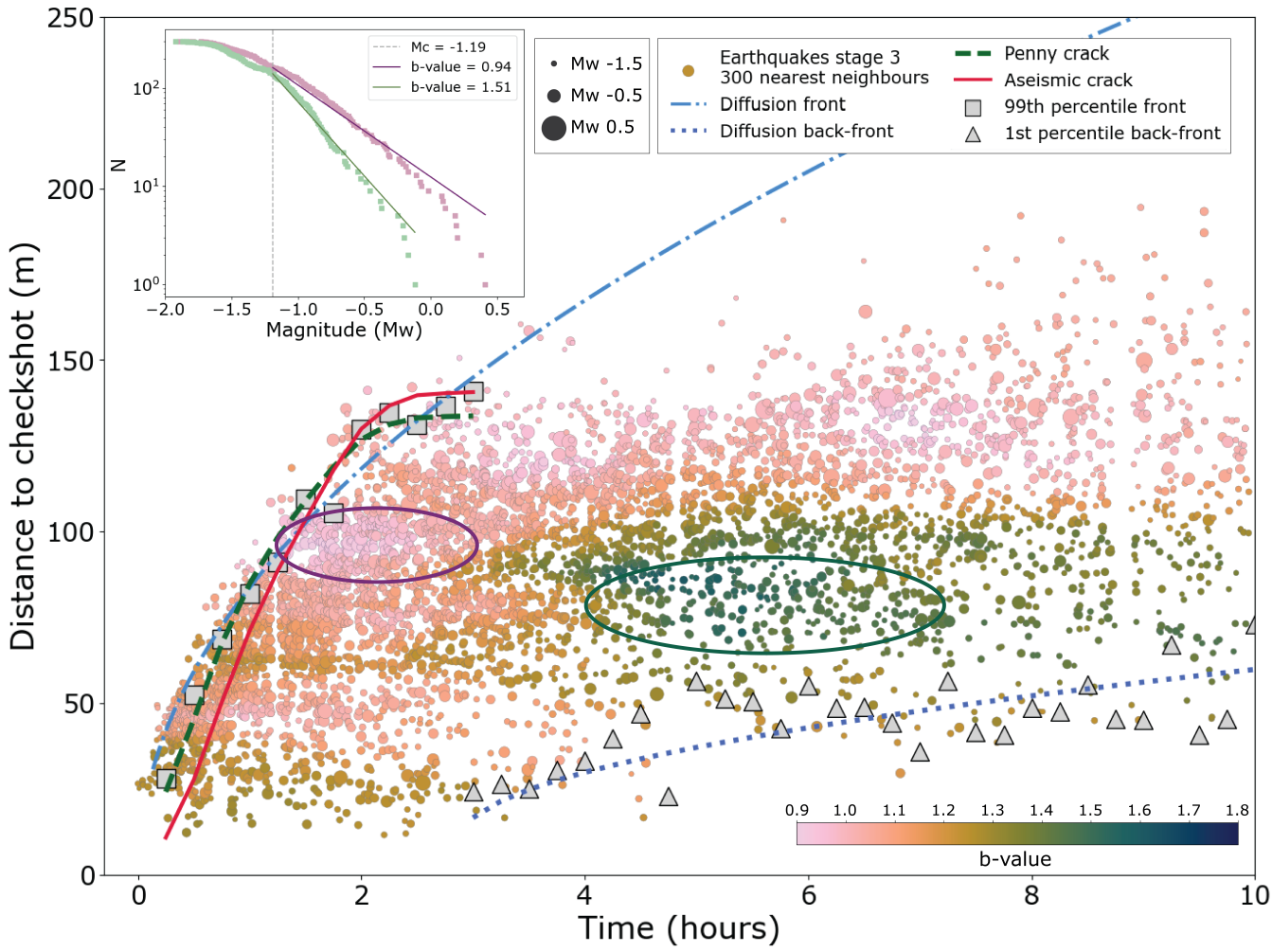

Figure 4 Time vs. distance plot and model fits. Circles are earthquakes and their size is proportional to magnitude. Distance is the 3D Euclidean distance calculated to the check-shot point. Gray squares are the 99th percentile of the earthquake front calculated until injection operations stop, binned every 15 minutes (see methods for details). Triangles are the 1st percentile of the earthquake back-front after injection stops, binned every 15 minutes. The ellipses in the main figure highlight the two subsets of 300 events for which a frequency-magnitude distribution is shown in the inlet (Mc fixed to that of the whole catalog).

However, indication of a propagating fracture is also supported by the presence of low *b*-values at the edges of the earthquake propagating front (Figure 4 and Figure S4) and a roll-off for large magnitude earthquakes in the magnitude-frequency distribution for large magnitude with respect to the fitted Gutenberg-Richter model (Figure 2a) (Passarelli et al., 2015). We caution that this analysis is not altogether conclusive, and we cannot rule out the hypothesis of slip on a fault with presumably aseismic slip involved.

4.3 Pseudo prospective forecasts

The spatio-temporal analysis of Stage 3 highlights that complex physical mechanisms are at play. The pressure evolution is most certainly affected also by the stimulation approach (e.g. open hole vs. perforations and slickwater vs. polymer fluid system with micro-proppants). Similarly, the evolution of seismicity could be further linked to stimulation approach, making it non-trivial to reproduce the evolution of seismicity rate, *b*-value, and spatial extent of seismicity. In order to keep simplicity in testing the models for time-dependent forecasting, we introduced physical processes in a gradual approach, with: (i) the Empirical model – EM, representing the basic approach (seismicity rate simply dependent on injection rate), (ii) a Physics-Informed Machine Learning – PI-ML, representing the potential link to pressure propagation, and (iii) a Stochastic Hybrid Hydro-mechanical – HM1D, that potentially accounts for stress changes. Although the models only aim at forecasting the seismicity rate, they do share some similarity with the spatial models presented earlier (Figure 4).

We run two pseudo-forecast tests, with a t_{learn} gradually increasing every 2 minutes and for the case of fixed Mc at -1.19 and Mc internally computed by the model based on the dataset at a given t_{learn}. Figure 5 shows the forecasted cumulative number of events and frequency-magnitude distribution at four select snapshots at different times (i.e., t_{learn} 14:30, 15:00, 15:30,

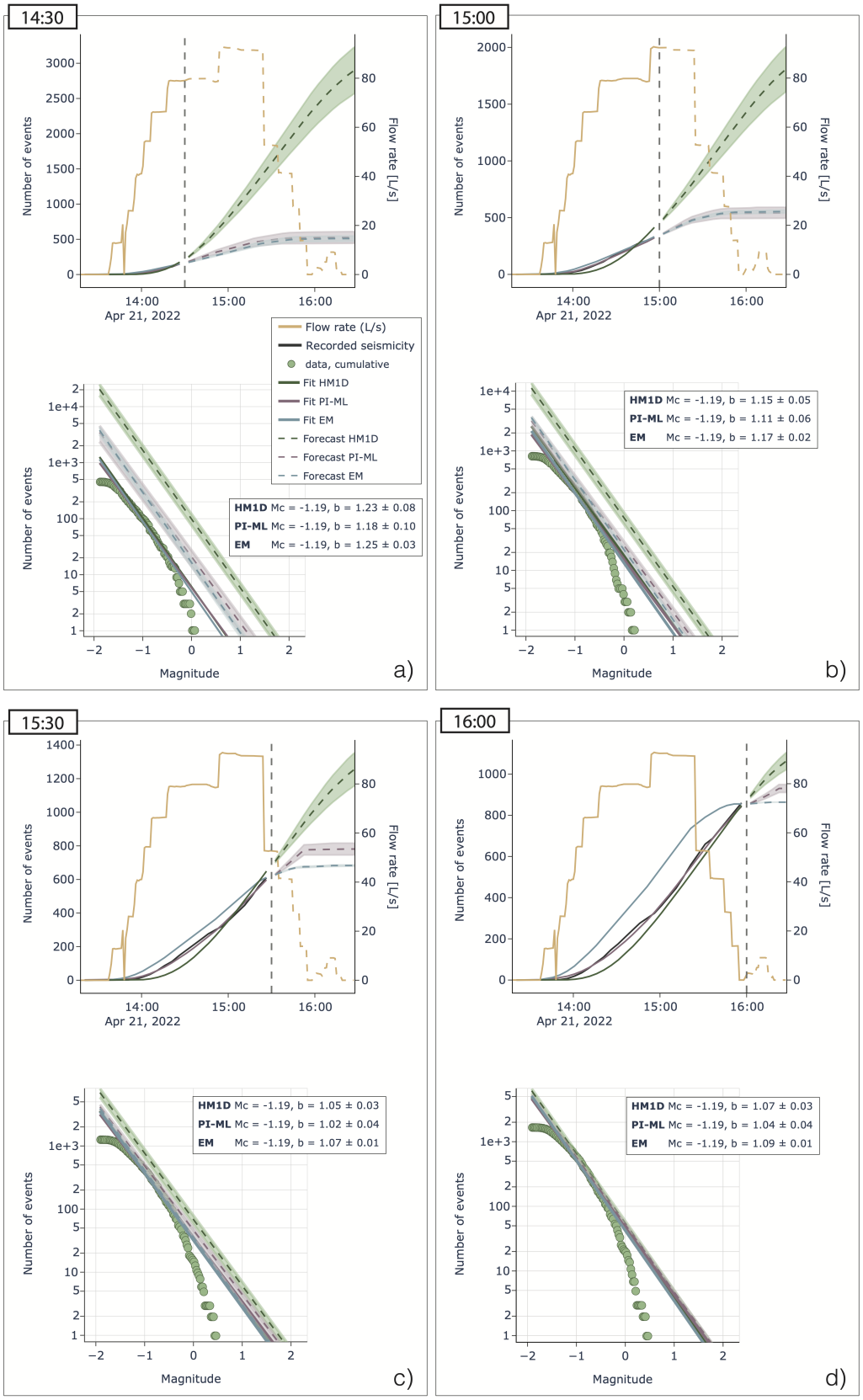

Figure 5 Four snapshots of the pseudo-forecast test with fixed Mc at different t_{learn} (14:30, 15:00, 15:30, 16:00 UTC). Each panel shows on top the cumulative number of events simulated and recorded before t_{learn} (black dashed – line) as well as the forecast cumulative number of events with stochastic variability in the shaded area (green HM1D, purple PI-ML, blue EM). The bottom of each panel compares the recorded frequency-magnitude distribution with the fitted curve at t_{learn} as well as the forecasted distribution at the end of the stimulation.

16:00 UTC) for the case of fixed Mc. For the case of variable Mc, we refer to Figure S8. At the beginning of the stimulation (t_{learn} = 14:30; Figure 5a), when few data points are available to calibrate the model, the HM1D model tends to predict a large number of events (about 2,700), while both EM and PI-ML predict only around 500 events. The estimated *b*-value is 1.23, 1.18, and 1.25 for HM1D, PI-ML, and EM, respectively. Figure 5b (t_{learn} = 15:00) shows similar trends, with the HM1D decreasing the final forecasted number of events to be closer to the measured one, and both PI-ML and EM only changing slightly. The forecasted *b*-value is 1.15, 1.11, and 1.17, for HM1D, PI-ML, and EM, respectively. Figure 5c (t_{learn} = 15:30) shows already results of models during the initial decrease of the flow rate: only the HM1D model predicts an increased number of events, while both PI-ML and EM models expect the seismicity rate to decrease substantially (hence no increase in total number of events). The forecasted *b*-value is at this time 1.05, 1.02, and 1.07, for HM1D, PI-ML, and EM, respectively. As new data are provided (Figure 5d; t_{learn} = 16:00), the PI-ML can predict a better decay of seismicity at a later stage, in a similar way to HM1D, and with forecasted *b*-value similar to the previous step as 1.07, 1.04, and 1.07, for HM1D, PI-ML, and EM, respectively. During the shut-in phase (Figure 5c-d), the EM performs particularly poorly at fitting the overall evolution of seismicity during the learning phase, with the model always overestimating the observed rate to achieve the cumulative number of events at t_{learn}.

While visually the four snapshots already provide a sense of the efficacy of the HM1D, a proper statistical comparison gives a better evaluation of the models' performance. Figure 6a and 6c show the models' performance for the pseudo-forecast test with fixed Mc at -1.19 for all the runs (i.e., with t_{learn} gradually increasing every 2 minutes). The main panel of Figure 6a shows the evolution of the cumulative log-likelihood, clearly indicating a better performance (i.e., smaller negative value) for the HM1D model after 1 hour from the start of injection. The bottom panels show the colored sequence representing the Probability Gain (PG) with respect to the model EM normalized for the best performing model. Dark green indicates the best performing model: with the exception of the first hour, the HM1D model performs much better when compared to EM, while the forecasting performance of PI-ML is only slightly better than EM.

Figure 6c shows the generalized N-test, with the main panel showing the forecasted number of events at each t_{learn} for all models (green HM1D, purple PI-ML, blue EM) with the horizontal black dotted line indicating the final observed number of events. The bottom panels show all cases whether the median forecasted number of events falls within a 95% confidence interval, with blue indicating that at the given t_{learn} the models forecast exactly the observed final number of events (i.e., 50% of an empirical cumulative distribution function - ECDF). Red color indicates a failed N-test. Results show that only the HM1D model can forecast the final number of events above magnitude of completeness, mostly within the 95% confidence interval, while both EM and PI-ML tend to underestimate the final number of recorded events and with a too small variable around the median value.

Figures 6b and d show the statistical test for the case when the models are free to calculate Mc at t_{learn}. Results are somewhat similar to the previous case, although illustrates how simple models requires less data to get closer to the final observed cumulative number of events (only 0.5 hours for EM and PI-ML compared to more than 1 hour for HM1D). However, even the case of variable Mc shows that the HM1D model clearly performs better during the decrease of the flow rate.

5 Discussion

5.1 Inferences of seismicity mechanisms from stimulation

For Stage 3 of the 2022 stimulation at Utah FORGE, the space and time distribution of earthquakes in Figure 4 would suggest, with no clear winner, either seismicity induced by an expanding hydro-fracture (tensile crack), or aseismic and seismic slip on an already existing fault. For further discrimination, it is important to consider the geometrical characteristics of the distribution of earthquake hypocenters with respect to the stress field measured at the injection site.

A hydro-fracture, generated from the injection operation in the local stress field configuration, opens in the direction of S_{Hmin} and expands in the S_v and S_{Hmax} directions either for a normal or strike-slip stress regime. A tensile dislocation plane is expected to be parallel to the S_v and S_{Hmax} plane and opening orthogonal to S_{Hmin}, therefore generally compatible with the geometry of the fitted plane from PCA, even in a scenario with the rotation of the stress field discussed in Xing et al. (2022). The seismicity triggered at the expanding crack edges occurs on optimally oriented faults at a certain angle from the edges of the tensile fracture plane. This angle depends on the friction properties and forms on wing-like bands of seismicity in 2D (Hill, 1977) or in 3D on a nearly hyperbolic surface (Passarelli et al., 2015) adjoining the tensile fractures. The planar configuration in Figure 3, the presence of wing-like lobes of seismicity at a different depth, the upward and sideward migration sub-parallel to S_v and S_{Hmax}, with little spreading in the orthogonal direction, and the further migration in the post-injection phase are all indicative of seismicity due to hydrofracturing (Schultz et al., 2020). Furthermore, the expected spatial and temporal evolution of the earthquake hypocenters in a time-distance diagram is characterized by a seismicity migration front and a back-front where minor or no earthquake activity occurs (Dahm et al., 2010), and thus compatible with the migration pattern depicted in Figure 4. The gradual increase of magnitude of events during the injection (Figure 3a and S7) and the minor migration in the post-injection phase, where also larger magnitude events occurred (Figure 3a and 4), are in line with the proposed correlation between seismic moment and tensile-crack volumes often found for dike intrusions in volcanic regions (Grandin et al., 2011; White and Mc-

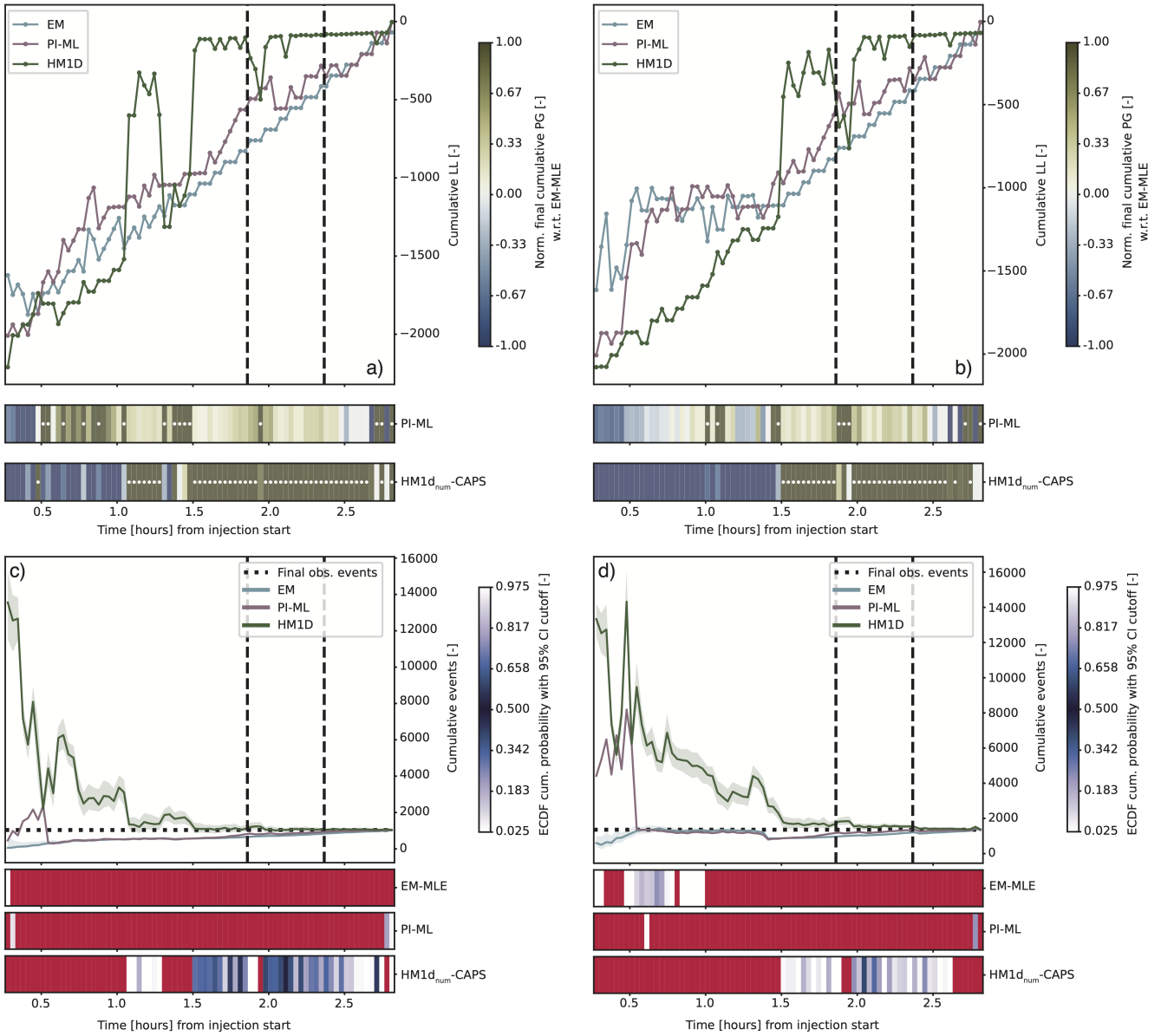

Figure 6 Cumulative log-likelihood, probability gain with respect to EM, and generalized N-test for the pseudo-forecast test with fixed Mc (panels a and c) and with variable Mc (panels b and d). Green HM1D, purple PI-ML, and blue EM. Vertical dashed lines indicate the period when the flow rate was decreased. Horizontal dashed line in panels c and d indicates the final number of observed events.

Causland, 2016). Additionally, the 40-50 MPa of pressure reached at the injection interval (Figure 3a) at the beginning of the injection operation (roughly for the first hour), equates or exceeds the magnitude of S_{Hmin} and it is compatible with the formation of a hydro-fracture. The subsequent drop of pressure at the peak of the flow rate is more complex to univocally interpret, with possible explanations as an indication of leak-off of fluids from the hydro-fracture or a depressurization due to the increase in the volume of the hydro-fracture. Correspondingly, the circulation phase that occurred after Stage 3 also injected at pressures above the hydraulics fracturing gradient. The available surface array data show that events induced by the circulation mostly cluster at the margins of the clouds induced during the main stimulation (Niemz et al., 2024).

In the scenarios of seismic and aseismic slip on one or more pre-existing faults, we assume that the fitted planar geometry can depict either a strike-slip or a normal fault, given the uncertainties on the determination of the in-situ stress field previously discussed. We further assume that slip occurs at first order on this simplified planar geometry and that the wing-lobes of seismicity described before can be considered as local complexities in the fault plane geometry. We use the Coulomb-Mohr failure criterion and Anderson's theory of faulting to assess the condition under which the slip can occur on the fitted plane for a normal or a strike-slip fault (Lengliné et al., 2017; Petruccelli et al., 2019; Turcotte and Schubert, 2014). The fitted plane in Figure 3b, c has strike $s = 15°$ and dip $\delta = 80°$, and it is not optimally oriented with respect to the stress field discussed ear-

lier, where S_v = *(62-65) MPa,* S_{Hmin} = *(40-45) MPa,* and S_{Hmax} = *(47-78) MPa,* and S_{Hmax} has strike N25°E. In the normal faulting stress configuration ($S_v > S_{Hmax} > S_{Hmin}$), the optimally oriented fault plane has a dip angle of 60° for a friction coefficient of $f_s = 0.85$ and strike parallel to S_{Hmax}; while in strike-slip stress configuration ($S_{Hmax} > S_v > S_{Hmin}$), the optimally oriented fault plane has strike N0°E. From the Anderson theory of faulting (Turcotte and Schubert, 2014), we can calculate the friction angle for the geometry of the fitted plane for strike slip as $f_s = |\cot(2(\sigma - s))| = |\cot 2(-10)| = 2.75$ or for normal faulting $f_s = |\frac{1}{\tan 2\delta}| = 2.75$, in both cases a large frictional ratio is unphysical for the Earth rocks for low normal stress cases (Byerlee, 1978). The large value of the retrieved coefficient of friction indicates that either normal or strike-slip on the inferred structures can occur only under very low normal stress conditions which are not attained under normal hydrostatic pore-pressure. This near-zero effective normal stress condition can be attained when the injection pressure reached 40 MPa, circa 15 minutes after the start of the injection operation for both a strike-slip and a normal fault. Zero effective normal stress condition points to opening of a tensile fracture, suggesting that hydrofracturing could indeed be the most likely explanation of the seismicity at Utah FORGE 2022 stimulation. Detailed information on moment tensors would provide valuable constraints to the style of slip at Utah FORGE. While full moment tensors could not be retrieved, Rutledge et al. (2025) used P, Sv, and Sh polarities and amplitude ratios recorded on the deep borehole geophones to constrain 20 focal mechanisms. The inclusion of the amplitude ratios also helps to better constrain the focal mechanisms, where the combination of Sh/P and Sv/P ratios helps constrain the fault plane's strike and dip, respectively. The majority of focal mechanisms are strike-slip with a mean strike of N5°E ±8° closely aligned with the N15°E trend of the seismicity found in the PCA analysis. There is also a small subset of normal faulting mechanisms located at greater depths. The pattern of failure planes nearly aligned with the trend of the event cloud and S_{Hmax} direction is consistent with the observed microseismic shearing being closely associated with fluid driven crack growth (Hill, 1977; Passarelli et al., 2015).

Insights into the seismic response can also be derived from the *b*-value spatial and temporal evolution. Dynamic changes in the system can be associated with changes in the *b*-values and thus can be used as a diagnostic tool of the hydraulic fracturing processes at play during injection operations (Ritz et al., 2022). During Stage 3 at Utah FORGE, the low *b*-value at the edge of the propagation front (Figure 4) can also suggest the opening of a new fracture as it highlights areas of increased stress which are consistent with high stress concentrations at the tip of expanding cracks (Scholz, 2015). However, in the post-shut-in phase, the *b*-value trends are complex, with a peak of *b*-value of 1.5 ~1 hour after the occurrence of the larger magnitude event. This suggests that a simple pore-pressure diffusion is not the only mechanism at the origin of the recorded seismicity. Although it is difficult to draw conclusions simply from the *b*-value evolution, further growth of hydraulic fractures and flow/percolation of fluids through pre-existing fracture network after shut-in has been observed before in low permeability reservoirs, such as tight granitoid rocks (Niemz et al., 2021).

Overall, these interpretations are consistent with those from prior induced seismicity cases. Typically, induced earthquakes are observed on pre-existing faults with (near) critically-stressed orientations (Schoenball et al., 2018; Hennings et al., 2019). In wastewater disposal settings, smaller changes in pore pressure tend to reactivate the most susceptible faults first (Fan et al., 2019; Stokes et al., 2023). However, the hydraulic fracturing process aims to create a new fracture network. Thus, cases of induced seismicity caused by hydraulic fracturing tend to observe two types of seismic response (Schultz et al., 2017; Konstantinovskaya et al., 2021): those delineated perpendicular to the minimum stress direction (i.e., stimulated fractures) and those reactivated along critically-stressed orientations (i.e., fault reactivation). Stimulation into low permeability formations restricts pressure diffusion to along the fracture network, which has the potential to intersect pre-existing faults for reactivation (Galloway et al., 2018). In these cases, fault reactivation is often more problematic, as it is associated with larger magnitude events (Eaton et al., 2018; Wang et al., 2020). Overall, these concepts support our assertion that events at Utah FORGE are predominantly stimulated fractures. We note that an independent examination of the growth of earthquake magnitudes also concluded that fracture growth was the predominant mechanism for Stage 3 (Schultz et al., 2025).

5.2 Implications for forecasting and risk management

The complexity of the seismic response is also seen in the performance of the forecasting models. The empirical model (EM), which is based mainly on the fluid injection volume, is not as successful in forecasting the seismicity decay after shut-in. On the other hand, a physics-informed machine learning model (PI-ML) is shown to provide more reliable forecasts especially for the post-shut-in phase (Figure 5d). However, a model incorporating permeability changes (HM1D) strongly outperforms the simplified approach, and it is capable of correctly forecasting the observed seismicity rate and cumulative number of events, especially during the flow rate reduction, although more data are needed before reliable results are achieved (~1 hour for the given dataset, Figure 6). The prediction of the post-injection/trailing seismicity is paramount for managing induced seismicity risks (Schultz et al., 2022). In the context of ATLP, where real-time data and seismicity forecasting models are used to estimate the seismic risk and to plan decision-making policies, forecasting models need to be computationally efficient while physically sound (Grigoli et al., 2017; Mignan et al., 2017; Broccardo et al., 2019). All the models tested here are capable of running much faster than the time in between t_{learn} (i.e. less than 2 minutes). The pseudo-forecast tests in the current work were run on a basic laptop, and on average both EM and

PI-ML models take only a few seconds, while HM1D, depending on the amount of data to invert, takes between 30 and 100 seconds for the current setup. More details about the model performance can be found in Clasen Repollés et al. (2025) that clearly demonstrated the usability of HM1D for real-time application and for different scales. It is worth noting that EM could be improved by imposing an exponential decay of the seismicity rate at the start of the decreasing flow rate sequence: this would increase the final forecasted number of events and would allow the model to successfully pass the generalized N-test, at least during the active injection phase (Figure 13c in Clasen Repollés et al., 2025). Also, the EM model employed here follows the simplified Maximum Likelihood Estimate (MLE) method to infer the model parameters, while a full Bayesian approach would provide a more variable distribution, hence statistically performing much better than MLE (Clasen Repollés et al., 2025).

While HM1D does not include all the physical mechanisms that could have caused the seismicity during Stage 3 of the Utah FORGE 2022 stimulation (namely tensile and aseismic crack development), the results of the pseudo-forecast tests clearly show that adding more physics can provide a better forecast. It is worth noting, however, that the model requires a very large number of parameters, which in real-time would not be trivial to estimate with a global inversion. The model was developed by Clasen Repollés et al. (2025), bearing in mind the applicability in real-time, hence the inversion approach based on differential evolutionary algorithm is limited in the parameter space as a global search of minima would require much longer computation time.

In this sense, we argue that the Stochastic hydromechanical model proposed by Clasen Repollés et al. (2025) shows great potential in an operational setting, meeting both the requirements of speed and robustness of the forecast as physics (namely permeability changes) strongly controls the evolution of flow rate and pressure, and subsequently generation of seismicity. However, it is important also to note the flexibility of a PI-ML approach: a future generation of the model could, for example, embed the same flow rate model based on a 1D numerical implementation including permeability changes and it could be extended to a 1D radial profile as HM1D. This would provide a LASSO model with a better evolution of pressure in space, and potentially similar forecasting capability as HM1D but with a strongly reduced number of parameters to calibrate and hence more flexibility of use in real-time. However, it is worth mentioning that here we used a seismicity catalog that went through several manual and automatic checks (Dyer et al., 2023b). Unfortunately, real-time catalogs often present artefacts that could strongly affect the forecasting capability of any model.

6 Conclusions

Our work demonstrates that a comparison between the stress field, hydraulic parameters, and spatio-temporal distribution of the seismicity cloud is key to constraining the triggering mechanism of seismicity. The study of the seismic response of the reservoir during the 2022 stimulation suggests that most likely a new hydraulic fracture opened in Stage 3 as a result of high-pressure injection. Empirical statistical seismicity rate models were able to adequately forecast the evolution of seismicity until the shut-in phase. Afterwards, a better physics-based understanding is to be integrated into the models in order to reproduce the observed seismic response. This is possible through machine learning models, where speed, needed for real-time performance, can be combined with assumptions of physical processes.

We demonstrate that a pathway to adoption of ATLP based on data-driven and physics-based forecasting models is now within reach, assuming the entire seismicity processing (waveform to catalog) is accurate. This marks an important step towards improving real-time risk mitigation strategies and making future EGS projects safer and more socially accepted.

Acknowledgments

This work is supported by the De-Risking Enhanced Geothermal Energy Projects (Innovation for DEEPs). DEEP is subsidized through the Cofund GEOTHERMICA by the Swiss Federal Office of Energy (SFOE), which is supported by the European Union's HORIZON 2020 programme for research, technological development, and demonstration under Grant Agreement #731117. Victor Clasen Repollés was supported under the grant: "Characterizing and understanding Enhanced Geothermal Systems (EGS) - novel tools and applications in deep underground laboratory" (SNSF Project no. 200021_197366/1). The authors thanks Maria Mesimeri for useful discussion and input on the moment tensor inversion. We thank the editor Giuseppe Petrillo and two anonymous reviewers, whose comments helped improve this manuscript. Last, we also acknowledge the U.S. Department of Energy for making the data publicly available through the Geothermal Data Repository (GDR: https://gdr.openei.org/forge).

7 Competing interests

The authors declare no competing interests.

8 Data and Code Availability

Data from the Utah FORGE stimulations are available through the Geothermal Data Repository (https://gdr.openei.org/forge). The downhole catalog of Dyer et al. (2023b) is available through the ISC Dataset repository accessible via https://doi.org/10.31905/52CC4QZB. The statistical analysis was performed using the SeismoStats package, available in github: https://github.com/swiss-seismological-service/SeismoStats. The PCA analysis was carried out using the singular value decomposition (*svd*) routine in MATLAB. Similarly, the fits for the fracturing mechanism models were obtained using the nonlinear

least squares fitting option in MATLAB. All model equations are provided in the Methods section to ensure reproducibility. The supplementary video (Movie S1) is available at the ETH Research Collection at: https://doi.org/10.3929/ethz-c-000785663. The configuration files for the pseudo-forecasting runs and snapshots of the codes for the forecasting models and orchestrator RT-HERMES are also available at the ETH Research Collection: https://doi.org/10.3929/ethz-c-000785633.

References

Bachmann, C. E., Wiemer, S., Woessner, J., and Hainzl, S. Statistical analysis of the induced Basel 2006 earthquake sequence: introducing a probability-based monitoring approach for Enhanced Geothermal Systems. *Geophysical Journal International*, 186(2): 793–807, June 2011. doi: 10.1111/j.1365-246x.2011.05068.x.

Barton, N., Bandis, S., and Bakhtar, K. Strength, deformation and conductivity coupling of rock joints. *International Journal of Rock Mechanics and Mining Sciences & Geomechanics Abstracts*, 22(3):121–140, June 1985. doi: 10.1016/0148-9062(85)93227-9.

Broccardo, M., Mignan, A., Wiemer, S., Stojadinovic, B., and Giardini, D. Hierarchical Bayesian Modeling of Fluid-Induced Seismicity. *Geophysical Research Letters*, 44(22), Nov. 2017. doi: 10.1002/2017gl075251.

Broccardo, M., Mignan, A., Grigoli, F., Karvounis, D., Rinaldi, A. P., Danciu, L., Hofmann, H., Milkereit, C., Dahm, T., Zimmermann, G., Hjörleifsdóttir, V., and Wiemer, S. Induced seismicity risk analysis of the hydraulic stimulation of a geothermal well on Geldinganes, Iceland. Nov. 2019. doi: 10.5194/nhess-2019-331.

Byerlee, J. Friction of rocks. *pure and applied geophysics*, 116(4–5): 615–626, July 1978. doi: 10.1007/bf00876528.

Cappa, F., Scuderi, M. M., Collettini, C., Guglielmi, Y., and Avouac, J.-P. Stabilization of fault slip by fluid injection in the laboratory and in situ. *Science Advances*, 5(3), Mar. 2019. doi: 10.1126/sciadv.aau4065.

Clasen Repollés, V., Rinaldi, A. P., Ciardo, F., Passarelli, L., Karvounis, D., and Wiemer, S. Development of 1D Hybrid Hydromechanical Models for Real-Time Forecasting of Induced Seismicity Rate. *Journal of Geophysical Research: Solid Earth*, 130(8), Aug. 2025. doi: 10.1029/2025jb031592.

Dahm, T., Hainzl, S., and Fischer, T. Bidirectional and unidirectional fracture growth during hydrofracturing: Role of driving stress gradients. *Journal of Geophysical Research: Solid Earth*, 115(B12), Dec. 2010. doi: 10.1029/2009jb006817.

Danré, P., Garagash, D., De Barros, L., Cappa, F., and Ampuero, J. Control of Seismicity Migration in Earthquake Swarms by Injected Fluid Volume and Aseismic Crack Propagation. *Journal of Geophysical Research: Solid Earth*, 129(1), Jan. 2024. doi: 10.1029/2023jb027276.

Davis, T., Rivalta, E., and Dahm, T. Critical fluid injection volumes for uncontrolled fracture ascent. Feb. 2020. doi: 10.31223/osf.io/z4g8n.

Dyer, B., Bethmann, F., Karvounis, D., Meier, P., Pankow, K., Wannamaker, P., Moore, J., Rutledge, J., and Ammon, A. Innovative microseismic monitoring tools and configurations for geothermal applications. In *Proceedings of the World Geothermal Congress*, page 11, Beijing, China, 2023a.

Dyer, B., Karvounis, D., and Bethmann, F. Microseismic event catalogues from the well 16A(78)-32 stimulation in April, 2022 in Utah FORGE., Oct. 2023b. doi: 10.31905/52cc4qzb.

Eaton, D. W., Igonin, N., Poulin, A., Weir, R., Zhang, H., Pellegrino, S., and Rodriguez, G. Induced Seismicity Characterization during Hydraulic-Fracture Monitoring with a Shallow-Wellbore Geophone Array and Broadband Sensors. *Seismological Research Letters*, 89(5):1641–1651, July 2018. doi: 10.1785/0220180055.

Fan, Z., Eichhubl, P., and Newell, P. Basement Fault Reactivation by Fluid Injection Into Sedimentary Reservoirs: Poroelastic Effects. *Journal of Geophysical Research: Solid Earth*, 124(7):7354–7369, July 2019. doi: 10.1029/2018jb017062.

Galloway, E., Hauck, T., Corlett, H., Pană, D., and Schultz, R. Faults and associated karst collapse suggest conduits for fluid flow that influence hydraulic fracturing-induced seismicity. *Proceedings of the National Academy of Sciences*, 115(43), Oct. 2018. doi: 10.1073/pnas.1807549115.

Grandin, R., Jacques, E., Nercessian, A., Ayele, A., Doubre, C., Socquet, A., Keir, D., Kassim, M., Lemarchand, A., and King, G. C. P. Seismicity during lateral dike propagation: Insights from new data in the recent Manda Hararo–Dabbahu rifting episode (Afar, Ethiopia). *Geochemistry, Geophysics, Geosystems*, 12(4), Apr. 2011. doi: 10.1029/2010gc003434.

Grigoli, F., Cesca, S., Priolo, E., Rinaldi, A. P., Clinton, J. F., Stabile, T. A., Dost, B., Fernandez, M. G., Wiemer, S., and Dahm, T. Current challenges in monitoring, discrimination, and management of induced seismicity related to underground industrial activities: A European perspective. *Reviews of Geophysics*, 55 (2):310–340, Apr. 2017. doi: 10.1002/2016rg000542.

Grigoratos, I., Savvaidis, A., and Rathje, E. Distinguishing the Causal Factors of Induced Seismicity in the Delaware Basin: Hydraulic Fracturing or Wastewater Disposal? *Seismological Research Letters*, 93(5):2640–2658, June 2022. doi: 10.1785/0220210320.

Guglielmi, Y., Cappa, F., Avouac, J.-P., Henry, P., and Elsworth, D. Seismicity triggered by fluid injection–induced aseismic slip. *Science*, 348(6240):1224–1226, June 2015. doi: 10.1126/science.aab0476.

Gwynn, M., Allis, R., Hardwick, C., Hill, J., and Moore, J. A new look at the thermal regime around Roosevelt Hot Springs, Utah. *GRC Transactions*, 40:551–558, 2016.

Hennings, P. H., Lund Snee, J., Osmond, J. L., DeShon, H. R., Dommisse, R., Horne, E., Lemons, C., and Zoback, M. D. Injection-Induced Seismicity and Fault-Slip Potential in the Fort Worth Basin, Texas. *Bulletin of the Seismological Society of America*, 109(5):1615–1634, July 2019. doi: 10.1785/0120190017.

Hill, D. P. A model for earthquake swarms. *Journal of Geophysical Research*, 82(8):1347–1352, Mar. 1977. doi: 10.1029/jb082i008p01347.

Horne, R., Genter, A., McClure, M., Ellsworth, W., Norbeck, J., and Schill, E. Enhanced geothermal systems for clean firm energy generation. *Nature Reviews Clean Technology*, 1(2):148–160, Jan. 2025. doi: 10.1038/s44359-024-00019-9.

Häring, M. O., Schanz, U., Ladner, F., and Dyer, B. C. Characterisation of the Basel 1 enhanced geothermal system. *Geothermics*, 37(5):469–495, Oct. 2008. doi: 10.1016/j.geothermics.2008.06.002.

Jia, Y., Tsang, C.-F., Hammar, A., and Niemi, A. Hydraulic stimulation strategies in enhanced geothermal systems (EGS): a review. *Geomechanics and Geophysics for Geo-Energy and Geo-Resources*, 8(6), Nov. 2022. doi: 10.1007/s40948-022-00516-w.

Jolliffe, I. T. and Cadima, J. Principal component analysis: a review and recent developments. *Philosophical Transactions of the Royal Society A: Mathematical, Physical and Engineering Sciences*, 374(2065):20150202, Apr. 2016. doi: 10.1098/rsta.2015.0202.

Jones, C., England, K., Simmons, S., Rose, P., Mella, M., Barker, B.,

McLennan, J., and Moore, J. Stimulation, Tracers and Geochemistry at Utah FORGE. In *PROCEEDINGS of the 48th Workshop on Geothermal Reservoir Engineering*, page – –224, Stanford, California, USA, 2023. Stanford University.

Jones, C., Simmons, S., and Moore, J. Geology of the Utah Frontier Observatory for Research in Geothermal Energy (FORGE) Enhanced Geothermal System (EGS) Site. *Geothermics*, 122: 103054, Sept. 2024. doi: 10.1016/j.geothermics.2024.103054.

Jordan, M. I. and Mitchell, T. M. Machine learning: Trends, perspectives, and prospects. *Science*, 349(6245):255–260, July 2015. doi: 10.1126/science.aaa8415.

Király-Proag, E., Gischig, V., Zechar, J. D., and Wiemer, S. Multicomponent ensemble models to forecast induced seismicity. *Geophysical Journal International*, 212(1):476–490, Sept. 2017. doi: 10.1093/gji/ggx393.

Konstantinovskaya, E., Li, Q., Zhmodik, A., Ibelegbu, C., Schultz, R., and Shipman, T. Lateral fluid propagation and strike slip fault reactivation related to hydraulic fracturing and induced seismicity in the Duvernay Formation, Fox Creek area, Alberta. *Geophysical Journal International*, 227(1):518–543, June 2021. doi: 10.1093/gji/ggab234.

Kwiatek, G., Martínez-Garzón, P., Goebel, T., Bohnhoff, M., Ben-Zion, Y., and Dresen, G. Intermittent Criticality Multi-Scale Processes Leading to Large Slip Events on Rough Laboratory Faults. *Journal of Geophysical Research: Solid Earth*, 129(3), Mar. 2024. doi: 10.1029/2023jb028411.

Lengliné, O., Boubacar, M., and Schmittbuhl, J. Seismicity related to the hydraulic stimulation of GRT1, Rittershoffen, France. *Geophysical Journal International*, page ggw490, Jan. 2017. doi: 10.1093/gji/ggw490.

Majer, E. L., Baria, R., Stark, M., Oates, S., Bommer, J., Smith, B., and Asanuma, H. Induced seismicity associated with Enhanced Geothermal Systems. *Geothermics*, 36(3):185–222, June 2007. doi: 10.1016/j.geothermics.2007.03.003.

Marzocchi, W. and Sandri, L. A review and new insights on the estimation of the b-value and its uncertainty. *Annals of Geophysics*, 46(6), Dec. 2009. doi: 10.4401/ag-3472.

McLennan, J., England, K., Rose, P., Moore, J., and Barker, B. Stimulation of a High-Temperature Granitic Reservoir at the Utah FORGE Site. In *SPE Hydraulic Fracturing Technology Conference and Exhibition*, 23HFTC. SPE, Jan. 2023. doi: 10.2118/212346-ms.

Mignan, A., Broccardo, M., Wiemer, S., and Giardini, D. Induced seismicity closed-form traffic light system for actuarial decision-making during deep fluid injections. *Scientific Reports*, 7(1), Oct. 2017. doi: 10.1038/s41598-017-13585-9.

Mignan, A., Karvounis, D., Broccardo, M., Wiemer, S., and Giardini, D. Including seismic risk mitigation measures into the Levelized Cost Of Electricity in enhanced geothermal systems for optimal siting. *Applied Energy*, 238:831–850, Mar. 2019. doi: 10.1016/j.apenergy.2019.01.109.

Mignan, A., Rinaldi, A. P., Lanza, F., and Wiemer, S. A Multi-LASSO model to forecast induced seismicity at enhanced geothermal systems. *Geoenergy Science and Engineering*, 236:212746, May 2024. doi: 10.1016/j.geoen.2024.212746.

Mirwald, A., Schmid, N., Han, M., Rohnacher, A., Mizrahi, L., Ritz, V., and Wiemer, S. SeismoStats: A Python Package for Statistical Seismology, 2025. https://github.com/swiss-seismological-service/SeismoStats.

Moein, M. J. A., Langenbruch, C., Schultz, R., Grigoli, F., Ellsworth, W. L., Wang, R., Rinaldi, A. P., and Shapiro, S. The physical mechanisms of induced earthquakes. *Nature Reviews Earth & Environment*, 4(12):847–863, Dec. 2023. doi: 10.1038/s43017-023-00497-8.

Moore, J., McLennan, J., Allis, R., Pankow, K., Simmons, S., Podgorney, R., Wannamaker, P., and Rickard, W. The Utah frontier observatory for research in geothermal energy (FORGE): An international laboratory for enhanced geothermal system technology development. In *PROCEEDINGS of the 44th Workshop on Geothermal Reservoir Engineering*, page – –214, Stanford, California, USA, 2019. Stanford University.

Moore, J., McLennan, J., Pankow, K., Finnila, A., Dyer, B., Karvounis, D., Bethmann, F., Podgorney, R., Rutledge, J., Meir, P., Xing, P., Jones, C., Barker, B., Simmons, S., and Damjanac, B. Current Activities at the Utah Frontier Observatory for Research in Geothermal Energy (FORGE): A Laboratory for Characterizing, Creating and Sustaining Enhanced Geothermal Systems. In *57th U.S. Rock Mechanics/Geomechanics Symposium*, ARMA23. ARMA, June 2023. doi: 10.56952/arma-2023-0749.

Möri, A. and Lecampion, B. Three-dimensional buoyant hydraulic fractures: finite-volume release. *Journal of Fluid Mechanics*, 972, Oct. 2023. doi: 10.1017/jfm.2023.711.

Niemz, P., Dahm, T., Milkereit, C., Cesca, S., Petersen, G., and Zang, A. Insights Into Hydraulic Fracture Growth Gained From a Joint Analysis of Seismometer-Derived Tilt Signals and Acoustic Emissions. *Journal of Geophysical Research: Solid Earth*, 126(12), Dec. 2021. doi: 10.1029/2021jb023057.

Niemz, P., McLennan, J., Pankow, K. L., Rutledge, J., and England, K. Circulation experiments at Utah FORGE: Near-surface seismic monitoring reveals fracture growth after shut-in. *Geothermics*, 119:102947, May 2024. doi: 10.1016/j.geothermics.2024.102947.

Nikkhoo, M., Walter, T. R., Lundgren, P. R., and Prats-Iraola, P. Compound dislocation models (CDMs) for volcano deformation analyses. *Geophysical Journal International*, 208(2):877–894, Nov. 2016. doi: 10.1093/gji/ggw427.

Olasolo, P., Juárez, M., Morales, M., D´Amico, S., and Liarte, I. Enhanced geothermal systems (EGS): A review. *Renewable and Sustainable Energy Reviews*, 56:133–144, Apr. 2016. doi: 10.1016/j.rser.2015.11.031.

Pankow, K., Mesimeri, M., Mclennan, J., Wannamaker, P., and Moore, J. Seismic monitoring at the Utah Frontier Observatory for research in geothermal energy. In *PROCEEDINGS of 45th Workshop on Geothermal Reservoir Engineering*, page – –216, Stanford, California, USA, 2020. Stanford University.

Parotidis, M., Rothert, E., and Shapiro, S. A. Pore-pressure diffusion: A possible triggering mechanism for the earthquake swarms 2000 in Vogtland/NW-Bohemia, central Europe. *Geophysical Research Letters*, 30(20), Oct. 2003. doi: 10.1029/2003gl018110.

Parotidis, M., Shapiro, S. A., and Rothert, E. Back front of seismicity induced after termination of borehole fluid injection. *Geophysical Research Letters*, 31(2), Jan. 2004. doi: 10.1029/2003gl018987.

Passarelli, L., Rivalta, E., Cesca, S., and Aoki, Y. Stress changes, focal mechanisms, and earthquake scaling laws for the 2000 dike at Miyakejima (Japan). *Journal of Geophysical Research: Solid Earth*, 120(6):4130–4145, June 2015. doi: 10.1002/2014jb011504.

Petruccelli, A., Schorlemmer, D., Tormann, T., Rinaldi, A., Wiemer, S., Gasperini, P., and Vannucci, G. The influence of faulting style on the size-distribution of global earthquakes. *Earth and Planetary Science Letters*, 527:115791, Dec. 2019. doi: 10.1016/j.epsl.2019.115791.

Quinn, D. P. and Ehlmann, B. L. A PCA-Based Framework for Determining Remotely Sensed Geological Surface Orientations and Their Statistical Quality. *Earth and Space Science*, 6(8): 1378–1408, Aug. 2019. doi: 10.1029/2018ea000416.

Ramadan, A., Gabry, M. A., Y. Soliman, M., and McLennan, J. Utah FORGE: A Decade of Innovation—Comprehensive Review of Field-Scale Advances (Part 1). *Processes*, 14(3):512, Feb. 2026. doi: 10.3390/pr14030512.

Rinaldi, A. P. and Nespoli, M. TOUGH2-seed: A coupled fluid flow and mechanical-stochastic approach to model injection-induced seismicity. *Computers & Geosciences*, 108:86–97, Nov. 2017. doi: 10.1016/j.cageo.2016.12.003.

Rinaldi, A. P. and Rutqvist, J. Joint opening or hydroshearing? Analyzing a fracture zone stimulation at Fenton Hill. *Geothermics*, 77:83–98, Jan. 2019. doi: 10.1016/j.geothermics.2018.08.006.

Ritz, V. A., Rinaldi, A. P., and Wiemer, S. Transient evolution of the relative size distribution of earthquakes as a risk indicator for induced seismicity. *Communications Earth & Environment*, 3(1), Oct. 2022. doi: 10.1038/s43247-022-00581-9.

Ritz, V. A., Mizrahi, L., Clasen Repollés, V., Rinaldi, A. P., Hjörleifsdóttir, V., and Wiemer, S. Pseudo-Prospective Forecasting of Induced and Natural Seismicity in the Hengill Geothermal Field. *Journal of Geophysical Research: Solid Earth*, 129(3), Mar. 2024. doi: 10.1029/2023jb028402.

Rutledge, J., Dyer, B., Bethmann, F., Meier, P., Pankow, K., Wannamaker, P., and Moore, J. Downhole Microseismic Monitoring of Injection Stimulations at the Utah FORGE EGS Site. In *56th U.S. Rock Mechanics/Geomechanics Symposium*, ARMA22. ARMA, June 2022. doi: 10.56952/arma-2022-0582.

Rutledge, J., K., N., P., D., B., and Karvounis, D. Microseismic source mechanisms during a Utah FORGE injection stimulation. In *PROCEEDINGS of 50th Workshop on Geothermal Reservoir Engineering*, page – –229, Stanford, California, USA, 2025. Stanford University.

Schmittbuhl, J., Lambotte, S., Lengliné, O., Grunberg, M., Jund, H., Vergne, J., Cornet, F., Doubre, C., and Masson, F. Induced and triggered seismicity below the city of Strasbourg, France from November 2019 to January 2021. *Comptes Rendus. Géoscience*, 353(S1):561–584, Jan. 2022. doi: 10.5802/crgeos.71.

Schoenball, M., Walsh, F. R., Weingarten, M., and Ellsworth, W. L. How faults wake up: The Guthrie-Langston, Oklahoma earthquakes. *The Leading Edge*, 37(2):100–106, Feb. 2018. doi: 10.1190/tle37020100.1.

Scholz, C. H. On the stress dependence of the earthquake b value. *Geophysical Research Letters*, 42(5):1399–1402, Mar. 2015. doi: 10.1002/2014gl062863.

Schultz, R., Wang, R., Gu, Y. J., Haug, K., and Atkinson, G. A seismological overview of the induced earthquakes in the Duvernay play near Fox Creek, Alberta. *Journal of Geophysical Research: Solid Earth*, 122(1):492–505, Jan. 2017. doi: 10.1002/2016jb013570.

Schultz, R., Skoumal, R. J., Brudzinski, M. R., Eaton, D., Baptie, B., and Ellsworth, W. Hydraulic Fracturing-Induced Seismicity. *Reviews of Geophysics*, 58(3), July 2020. doi: 10.1029/2019rg000695.

Schultz, R., Beroza, G. C., and Ellsworth, W. L. A risk-based approach for managing hydraulic fracturing–induced seismicity. *Science*, 372(6541):504–507, Apr. 2021. doi: 10.1126/science.abg5451.

Schultz, R., Ellsworth, W. L., and Beroza, G. C. Statistical bounds on how induced seismicity stops. *Scientific Reports*, 12(1), Jan. 2022. doi: 10.1038/s41598-022-05216-9.

Schultz, R., Lanza, F., Dyer, B., Karvounis, D., Fiori, R., Shi, P., Ritz, V., Villiger, L., Meier, P., and Wiemer, S. The bound growth of induced earthquakes could de-risk hydraulic fracturing. *Communications Earth & Environment*, 6(1), Nov. 2025. doi: 10.1038/s43247-025-02881-2.

Shapiro, S. A. *Fluid-Induced Seismicity*. Cambridge University Press, Apr. 2015. doi: 10.1017/cbo9781139051132.

Shapiro, S. A., Huenges, E., and Borm, G. Estimating the crust permeability from fluid-injection-induced seismic emission at the KTB site. *Geophysical Journal International*, 131(2):F15–F18, Nov. 1997. doi: 10.1111/j.1365-246x.1997.tb01215.x.

Shapiro, S. A., Dinske, C., Langenbruch, C., and Wenzel, F. Seismogenic index and magnitude probability of earthquakes induced during reservoir fluid stimulations. *The Leading Edge*, 29(3): 304–309, Mar. 2010. doi: 10.1190/1.3353727.

Stokes, S. M., Ge, S., Brown, M. R. M., Menezes, E. A., Sheehan, A. F., and Tiampo, K. F. Pore Pressure Diffusion and Onset of Induced Seismicity. *Journal of Geophysical Research: Solid Earth*, 128(3), Feb. 2023. doi: 10.1029/2022jb026012.

Tada, H., Paris, P. C., and Irwin, G. R. *The Stress Analysis of Cracks Handbook, Third Edition*. ASME Press, 2000. doi: 10.1115/1.801535.

Talwani, P. and Acree, S. Pore pressure diffusion and the mechanism of reservoir-induced seismicity. *pure and applied geophysics*, 122(6):947–965, Nov. 1984. doi: 10.1007/bf00876395.

Trutnevyte, E. and Wiemer, S. Tailor-made risk governance for induced seismicity of geothermal energy projects: An application to Switzerland. *Geothermics*, 65:295–312, Jan. 2017. doi: 10.1016/j.geothermics.2016.10.006.

Turcotte, D. and Schubert, G. *Geodynamics*. Cambridge University Press, Apr. 2014. doi: 10.1017/cbo9780511843877.

University of Utah. University of Utah Regional Seismic Network, 1962. doi: 10.7914/SN/UU.

Vaezi, I., Alcolea, A., Meier, P., Parisio, F., Carrera, J., and Vilarrasa, V. Numerical modeling of hydraulic stimulation of fractured crystalline rock at the bedretto underground laboratory for geosciences and geoenergies. *International Journal of Rock Mechanics and Mining Sciences*, 176:105689, Apr. 2024. doi: 10.1016/j.ijrmms.2024.105689.

Wang, J., Li, T., Gu, Y. J., Schultz, R., Yusifbayov, J., and Zhang, M. Sequential Fault Reactivation and Secondary Triggering in the March 2019 Red Deer Induced Earthquake Swarm. *Geophysical Research Letters*, 47(22), Nov. 2020. doi: 10.1029/2020gl090219.

Wannamaker, P., Simmons, S., Miller, J., Hardwick, C., Erickson, B., Bowman, S., Kirby, S., Feigl, K., and Moore, J. Geophysical activities over the Utah FORGE site at the outset of project phase 3. In *45th Workshop on geothermal reservoir engineering*, page 1–14. 2020.

Whidden, K., Petersen, G., and Pankow, K. Seismic Monitoring of the 2022 Utah FORGE stimulation: The view from the surface. In *PROCEEDINGS of the 48th Workshop on Geothermal Reservoir Engineering*, page – –224, 2023.

White, R. and McCausland, W. Volcano-tectonic earthquakes: A new tool for estimating intrusive volumes and forecasting eruptions. *Journal of Volcanology and Geothermal Research*, 309: 139–155, Jan. 2016. doi: 10.1016/j.jvolgeores.2015.10.020.

Wiemer, S. Minimum Magnitude of Completeness in Earthquake Catalogs: Examples from Alaska, the Western United States, and Japan. *Bulletin of the Seismological Society of America*, 90(4): 859–869, Aug. 2000. doi: 10.1785/0119990114.

Woessner, J. and Wiemer, S. Assessing the Quality of Earthquake Catalogues: Estimating the Magnitude of Completeness and Its Uncertainty. *Bulletin of the Seismological Society of America*, 95 (2):684–698, Apr. 2005. doi: 10.1785/0120040007.

Xing, P., Wray, A., Velez Arteaga, E., Finnila, A., Moore, J., Jones, C., Borchardt, E., and McLennan, J. In-situ Stresses and Fractures Inferred from Image Logs at Utah FORGE. In *47th Workshop on Geothermal Reservoir Engineering*. 2022.

Yu, P., Dempsey, D., Rinaldi, A. P., Calibugan, A., Ritz, V. A., and Archer, R. Association Between Injection and Microseismicity in Geothermal Fields With Multiple Wells: Data-Driven Modeling of Rotokawa, New Zealand, and Húsmúli, Iceland. *Journal of Geophysical Research: Solid Earth*, 128(4), Apr. 2023. doi: 10.1029/2022jb025952.

Zbinden, D., Rinaldi, A. P., Diehl, T., and Wiemer, S. Hydromechanical Modeling of Fault Reactivation in the St. Gallen Deep Geothermal Project (Switzerland): Poroelasticity or Hydraulic Connection? *Geophysical Research Letters*, 47(3), Feb. 2020. doi: 10.1029/2019gl085201.

Zhou, W., Lanza, F., Grigoratos, I., Schultz, R., Cousse, J., Trutnevyte, E., Muntendam-Bos, A., and Wiemer, S. Managing Induced Seismicity Risks From Enhanced Geothermal Systems: A Good Practice Guideline. *Reviews of Geophysics*, 62(4), Oct. 2024. doi: 10.1029/2024rg000849.

Zimmerman, R. and Bodvarsson, G. Hydraulic conductivity of rock fractures. *Transport in Porous Media*, 23(1), Apr. 1996. doi: 10.1007/bf00145263.